

How coherent are the vortices of two-dimensional turbulence?

Mohammad Farazmand^{1,2} and George Haller²

¹*Department of Mathematics, ETH Zurich, Switzerland*

²*Institute of Mechanical Systems, ETH Zurich, Switzerland*

(Dated: 30 June 2014)

We use recent developments in the theory of finite-time dynamical systems to locate the material boundaries of coherent vortices objectively in two-dimensional Navier–Stokes turbulence. We show that these boundaries are optimal in the sense that any closed curve in their exterior will lose coherence under material advection. Through a detailed comparison, we find that other available Eulerian and Lagrangian techniques significantly underestimate the size of each coherent vortex.

I. INTRODUCTION

Coherent vortices are persistent patches of rotating fluid that are observed in experimentally and numerically generated two-dimensional turbulence¹⁻⁴. As opposed to a typical closed material line, the boundary of a coherent vortex is envisioned to preserve its overall shape without substantial stretching, folding or filamentation⁵⁻⁷. While intuitive and simple, this material view on vortices has proven surprisingly challenging to implement in detecting vortex boundaries^{8,9}.

The formation and evolution of coherent fluid blobs is part of the material response of the fluid to external effects. By a classic axiom of continuum mechanics¹⁰, this material response should be objective, i.e., invariant with respect to time-dependent rotations and translations of the frame of the observer. Yet vorticity, the main diagnostic for structure identification in fluid mechanics, is not objective: it changes in coordinate systems rotating relative to each other, thus giving conflicting vortex definitions in different frames. Consequently, there is no well-justified threshold over which vorticity should necessarily mark a vortex.

To address this issue, a number of alternative Eulerian diagnostics have been proposed for vortex detection (see Jeong and Hussain¹¹ and Haller¹², for a review). For instance, the Okubo–Weiss (OW) criterion^{13,14} identifies vortices as regions where vorticity dominates strain. The Q -criterion offers a three-dimensional version of this principle¹⁵. In later work, Hua and Klein¹⁶ also include accelerations in the strain-vorticity comparison. Unfortunately, all these instantaneous diagnostics still lack objectivity, as well as a clearly derived mathematical connection to sustained material coherence. As a consequence, vortex boundaries suggested by instantaneous Eulerian diagnostics tend to lose their coherence rapidly under advection in unsteady flows¹⁷.

A recent development in the theory of finite-time dynamical systems⁶ offers an objective (frame-independent) and threshold-free Lagrangian approach to the identification of coherent vortices in two-dimensional flows. Specifically, Haller and Beron-Vera⁶ show that coherent (non-filamenting) material lines are necessarily stationary curves of an appropriately defined Lagrangian strain-energy functional. They solve this variational problem explicitly to uncover vortex boundaries as outermost limit cycles of a vector field derived from the invariants of the Cauchy–Green strain tensor. Haller and Beron-Vera⁶ demonstrate the efficacy of this approach by extracting maximally coherent Agulhas rings from satellite-derived

oceanic surface velocities.

Here, we use this method to detect the optimal boundaries of coherent vortices in a direct numerical simulation of Navier–Stokes turbulence. We also carry out a detailed comparison with alternative Eulerian and Lagrangian techniques. This comparison reveals that the coherent vortices that survive for long times are significantly larger than previously thought.

II. PRELIMINARIES

A. Set-up

Let $u(x, t)$ be a two-dimensional velocity field, defined over positions x in an open domain $U \subset \mathbb{R}^2$ and times t ranging through a finite interval $I = [a, b]$. We assume that $u(x, t)$ is a continuously differentiable function of its arguments. The motion of passive fluid particles under such a velocity field is governed by the differential equation

$$\dot{x} = u(x, t), \tag{1}$$

where $x(t; t_0, x_0)$ is the position of a particle at time t whose initial position at time t_0 is $x_0 \in U$. For the fixed time interval I , the dynamical system (1) defines the flow map

$$\begin{aligned} F : U &\rightarrow U, \\ x_a &\mapsto x_b, \end{aligned} \tag{2}$$

which takes an initial condition x_a to its time- b position $x_b = F(x_a) := x(b; a, x_a)$. We recall from the classic theory of ordinary differential equations that the flow map F is as smooth as the underlying velocity field u .¹⁸

B. Coherence principle

A typical set of fluid particles deforms significantly as advected under the flow map F , provided that the advection time $b - a$ is at least of the order of a few eddy turn-over times in a turbulent flow¹⁹. One may seek coherent material vortices as atypical sets of fluid trajectories that defy this trend by preserving their overall shape. These shapes are necessarily bounded by closed material lines that rotate and translate, but otherwise show no appreciable stretching or folding.

Haller and Beron-Vera⁶ seek Lagrangian vortex boundaries as closed material lines across which the averaged material straining shows no leading-order variability. Specifically, a thin material belt around a typical material line γ experiences visible inhomogeneity in straining under advection. A thin material belt around a coherent material line, however, does not exhibit leading-order inhomogeneity in its straining (see figure 1).

To formulate this observation mathematically, we let γ be a closed material line over the time interval $[a, b]$, and let $r : s \mapsto r(s)$, with $s \in [0, \sigma]$, be a parametrization of γ at the initial time $t = a$. The averaged tangential strain along γ , computed between the times a and b is then given by

$$Q(\gamma) = \frac{1}{\sigma} \int_0^\sigma \frac{\sqrt{\langle r'(s), C(r(s))r'(s) \rangle}}{\sqrt{\langle r'(s), r'(s) \rangle}} ds, \quad (3)$$

where the right Cauchy–Green strain tensor²⁰ $C = DF^\top DF$ is defined in terms of the Jacobian DF of the flow map; the symbol \top denotes matrix transposition; prime denotes differentiation with respect to the parameter s ; $\langle \cdot, \cdot \rangle$ denotes the Euclidean inner product. The integrand in equation (3) represents the pointwise tangential strain (see Haller and Beron-Vera⁶ for details).

Consider a small perturbation to γ given by $\gamma + \epsilon h$, where $0 < \epsilon \ll 1$ and $h : [0, \sigma] \rightarrow \mathbb{R}^2$ is a σ -periodic, $\mathcal{O}(1)$ vector field orthogonal to γ . The perturbation $\gamma + \epsilon h$ represents the thin material belt of figure 1. For a typical material line, we have $Q(\gamma + \epsilon h) = Q(\gamma) + \mathcal{O}(\epsilon)$ owing to the smoothness of the flow map F . That is, $\mathcal{O}(\epsilon)$ -perturbations to the material line γ lead to a $\mathcal{O}(\epsilon)$ -perturbation in the averaged tangential strain Q . Haller and Beron-Vera⁶ argue that for a thin material belt centered on γ to remain coherent, the belt should not show a leading-order change with respect to ϵ in its averaged straining. In other words, $Q(\gamma + \epsilon h) = Q(\gamma) + \mathcal{O}(\epsilon^2)$ should hold for γ , or equivalently, the first variation of Q should vanish on γ , i.e., $\delta Q(\gamma) = 0$.

The Euler-Lagrange equations arising from the condition $\delta Q(\gamma) = 0$ are too complicated to yield insight. Haller and Beron-Vera⁶ show, however, that a material line satisfies $\delta Q(\gamma) = 0$ if and only if it satisfies the pointwise condition

$$\langle r'(s), E_\lambda(r(s))r'(s) \rangle = 0, \quad (4)$$

for some constant $\lambda > 0$, with the generalized *Green–Lagrange strain tensor* E_λ defined as

$$E_\lambda = \frac{1}{2}[C - \lambda^2 I], \quad (5)$$

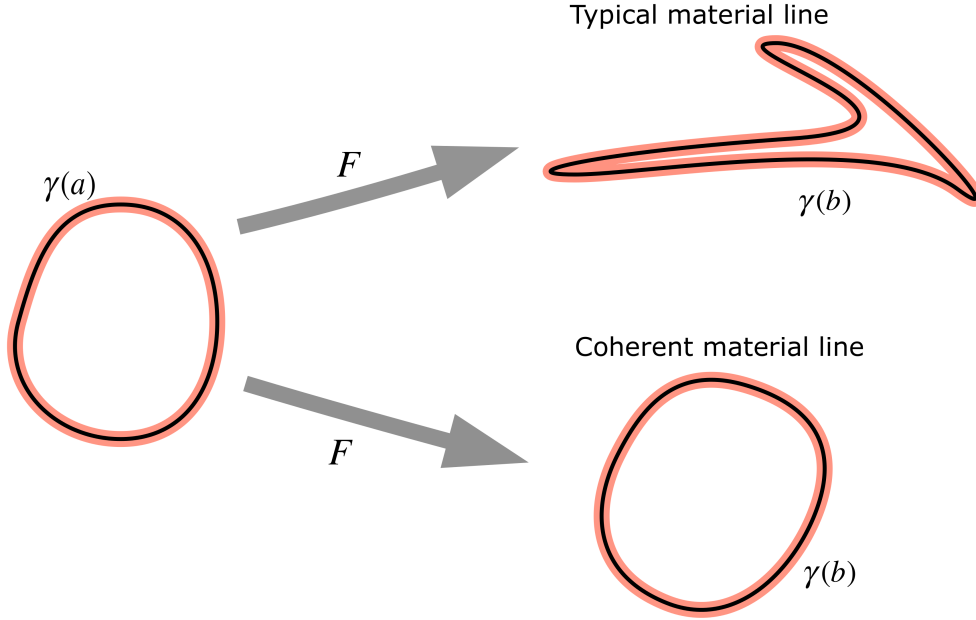


FIG. 1: Deformation of a typical material line γ versus a coherent material line as advected under the flow map F from time $t = a$ to $t = b$. No leading-order variation in the averaged stretching is observed in the material belt (red) around a coherent material line.

where I is the two-by-two identity matrix.

The implicit family of differential equations (4) is equivalent to two families of explicit differential equations of the form

$$r' = \eta_{\lambda}^{\pm}(r) := \sqrt{\frac{\lambda_2(r) - \lambda^2}{\lambda_2(r) - \lambda_1(r)}} \xi_1(r) \pm \sqrt{\frac{\lambda^2 - \lambda_1(r)}{\lambda_2(r) - \lambda_1(r)}} \xi_2(r), \quad (6)$$

where $0 < \lambda_1 \leq \lambda_2$ are eigenvalues of C and $\{\xi_1, \xi_2\}$ are their corresponding orthogonal eigenvectors⁶. In an incompressible flow, we have $\lambda_1 \lambda_2 = 1$ (see, e.g., Arnold¹⁸).

The vectors η_{λ}^{+} and η_{λ}^{-} are one-parameter families of vector fields with λ acting as the parameter. In an incompressible flow, we have $\lambda_2 \geq 1$ and $\lambda_1 \leq 1$. Therefore, for $\lambda = 1$, η_{λ}^{\pm} are well-defined real vector fields over the entire physical domain U . For $\lambda \neq 1$, the vector fields η_{λ}^{\pm} are only defined over a subset $U_{\lambda} \subset U$ where $\lambda_2 \geq \lambda^2$ and $\lambda_1 \leq \lambda^2$. The trajectories of η_{λ}^{\pm} can be computed over U_{λ} . We refer to these trajectories as λ -stretching material lines (or λ -lines, for short)

C. Lagrangian vortex boundaries and λ -lines

Here, we recall from Haller and Beron-Vera⁶ some properties of the λ -lines (i.e., trajectories of (6)), that are relevant for Lagrangian coherent vortex detection:

(i) *Uniform stretching*: λ -lines stretch uniformly by a factor of λ as advected under the flow map F . To quantify this statement, let γ_a be the time- a position of a λ -line parametrized by $r : s \mapsto r(s)$. Since γ_a is a λ -line, we have $r'(s) \parallel \eta_\lambda^\pm(r(s))$. Its time- b position γ_b will be parametrized by $F \circ r : s \mapsto F(r(s))$, whose tangent vector is given by $DF(r(s))r'(s)$. It is readily verifiable that $|DF(r(s))r'(s)| = \lambda|r'(s)|$. That is, each material element of γ_a stretches by a factor of λ as advected by the flow to time $t = b$. Consequently, such total length of any the curve also changes by a factor of λ , i.e. $\ell(\gamma_b) = \lambda\ell(\gamma_a)$, where ℓ is the length of the curve.

For $\lambda = 1$, this implies that the final length $\ell(\gamma_b)$ is equal to the initial length $\ell(\gamma_a)$, and hence the λ line exactly preserves its arclength. This is a highly atypical behavior in a turbulent flow, where a typical material line will stretch exponentially under advection. Yet through any point in the domain U , there will be precisely two material lines preserving their arclength between the times a and b . Such lines are computable as trajectories of the vector fields η_1^+ and η_1^- .

For $\lambda \neq 1$, a similar statement holds for the subset $U_\lambda \subset U$: Passing through any point in U_λ are two uniformly stretching material lines that stretch by a factor λ between the time a and b .

(ii) *Existence of closed λ -lines*: Although λ -lines fill the set U_λ , most of them are open curves. As shown in section §III, however, nested families of closed λ -lines do arise in two-dimensional turbulence. Members of such families corresponding to $\lambda = 1$ mark the highest possible degree of coherence in incompressible flows: both of their arclength and their enclosed area is preserved under material advection. Outermost members of closed λ -line families mark Lagrangian vortex boundaries, the largest possible closed curves that remain coherent under advection⁶.

(iii) *Relation to KAM tori*: In time-periodically perturbed, two-dimensional Hamiltonian systems, Kolmogorov–Arnold–Moser (KAM) curves are closed material lines that are mapped exactly into themselves by the flow in one time-period²¹. These curves, therefore, preserve both their arclength and their enclosed area in one time period, acting as archetyp-

ical coherent Lagrangian vortex boundaries. In a general, temporally aperiodic velocity field, closed material lines are no longer mapped into their original position for any choice of the advection time. A closed λ -line with $\lambda = 1$, however generalizes the notion of a KAM curve in a finite-time aperiodic flow, exhibiting both conservation of arclength and enclosed area between the initial and the final time. In the time-periodic case, closed λ -lines with $\lambda = 1$ become indistinguishable from KAM curves when extracted over a time that is a high enough multiple of the period^{22,23}.

In light of the above discussion, we seek Lagrangian coherent vortex boundaries as closed λ -lines. We refer to closed λ -lines as *elliptic Lagrangian coherent structures* (or elliptic LCSs, for short). In the case $\lambda = 1$, they are referred to as *primary* elliptic LCSs.

D. Metric interpretation and cosmological analogy

As pointed out in Haller and Beron-Vera⁶, elliptic LCSs bear a mathematical analogy with structures surrounding black holes in cosmology. Over the subset U_λ of the flow domain, the bilinear form

$$g_\lambda(v, w) = \langle v, E_\lambda w \rangle$$

defines a Lorentzian metric with signature $(-, +)$. The set U_λ equipped with this metric is a two-dimensional Lorentzian manifold or *space-time*²⁴. Unlike in Euclidean geometry, the distance between two distinct points of this space-time, as measured by its metric g_λ , can be negative or zero.

In the language of Lorentzian geometry, the λ -lines defined by (4) can be interpreted as closed null-geodesics of the metric g_λ .^{6,25} In cosmology, such surfaces of null-geodesics with closed space-like projections are called *photon spheres*.^{6,26} They are composed of periodic light orbits that encircle black holes.

An elliptic LCS, as any closed null-geodesic of the metric g_λ , must necessarily encircle at least two singularities of g_λ . This fact considerably simplifies the automated detection of elliptic LCSs in spatially complex flow data²⁵.

III. RESULTS AND DISCUSSION

We use the method described in section §II to identify coherent Lagrangian vortices in a direct numerical simulation of two-dimensional forced turbulence.

A. Numerical method

Consider the Navier–Stokes equations

$$\partial_t u + u \cdot \nabla u = -\nabla p + \nu \Delta u + f, \quad (7a)$$

$$\nabla \cdot u = 0, \quad (7b)$$

$$u(x, 0) = u_0(x), \quad (7c)$$

where the velocity field $u(x, t)$ is defined on the two-dimensional domain $U = [0, 2\pi] \times [0, 2\pi]$ with doubly periodic boundary conditions.

We use a standard pseudo-spectral method with 512 modes in each direction and 2/3 dealiasing to solve the above Navier–Stokes equation with viscosity $\nu = 10^{-5}$. The time integration is carried out over the interval $t \in [0, 50]$ (approximately, three eddy-turn-over times) by a fourth-order Runge-Kutta method with variable step-size²⁷. The initial condition u_0 is the velocity field of a decaying turbulent flow. The external force f is random in phase and band-limited, acting on the wave-numbers $3.5 < k < 4.5$. The forcing amplitude is time-dependent balancing the instantaneous enstrophy dissipation $\nu \int k^2 Z(k, t) dk$ where $Z(k, t) := \frac{1}{2} \int_{|\mathbf{k}|=k} |\hat{\omega}(\mathbf{k}, t)|^2 dS(\mathbf{k})$ with $\hat{\omega}(\cdot, t)$ being the Fourier transform of the instantaneous vorticity $\omega(\cdot, t) = \nabla \times u(\cdot, t)$.

In two dimensions, the energy injected into the system by the forcing is mostly transferred to larger scales through a nonlinear process^{28,29}. In order to prevent the energy accumulation at largest available scales over time, a linear damping is usually added to the Navier–Stokes equation to dissipate the energy at large scales^{30,31}. However, for the time scales considered here, the energy accumulation is not an issue and hence the linear damping will be omitted.

The theory reviewed in Section §II does not assume a particular governing equation for the velocity field $u(x, t)$. Thus, it can be applied to any two-dimensional velocity field, given as numerical solution of a partial differential equation or by direct measurements. In

particular, it can be applied to Lagrangian vortex detection for the solutions of the Navier–Stokes equation (7). To detect the Lagrangian vortex boundaries, we take the following steps:

1. Solve the Navier–Stokes equation (7) as discussed above to get the velocity field $u(x, t)$ over the time interval $t \in [0, 50]$ and a uniform 512×512 spatial grid over the domain $x \in U = [0, 2\pi] \times [0, 2\pi]$. The temporal resolution of the velocity field is 251 such that two consecutive time slices are $\Delta t = 0.2$ apart.
2. Advect each grid point according to the differential equation (1) from time $t = 0$ to time $t = 50$ to construct the flow map F such that $F(x_a) = x_b$ for any grid point x_a .
3. Construct an approximation of the deformation gradient DF by finite differences. To increase the finite difference accuracy, we use the auxiliary grid method introduced in Farazmand and Haller³². The chosen auxiliary grid distance is 10^{-3} .
4. Construct the right Cauchy–Green strain tensor $C(x_a) = [DF(x_a)]^\top DF(x_a)$ for each grid point x_a . Compute the eigenvalues $\{\lambda_1, \lambda_2\}$ and the corresponding eigenvectors $\{\xi_1, \xi_2\}$ of $C(x_a)$.
5. Seek closed orbits of the one-parameter families of vector fields η_λ^\pm defined in (6). For detecting these closed orbits, we use the automated algorithm developed in Haller and Beron-Vera⁶.

We detect the Lagrangian vortex boundaries as outermost elliptic LCSs, i.e., maximal limit cycles of η_λ^\pm . In the following, we present a detailed analysis of these vortex boundaries and compare them to those suggested by alternative Eulerian and Lagrangian indicators.

B. Lagrangian coherent vortex analysis

Figure 2a (left) shows the boundaries (red) of Lagrangian coherent vortices superimposed on the contours of the Eulerian vorticity (gray) at time $t = 0$. The boundaries are found as the outermost elliptic LCSs, i.e., maximal limit cycles of the vector fields η_λ^\pm (see Eq. (6)). The advected coherent vortex boundaries at time $t = 50$ are shown in figure 2a (right) along with the corresponding instantaneous vorticity field. By construction, these

Lagrangian vortex boundaries resist straining and filamentation under advection [see Fig. 2 (multimedia view)]. In the following, the vortex numbers refer to the numbering in figure 2a.

For basic reference, we also plot the zero level-curves of the most often used two-dimensional vortex diagnostic, the Okubo–Weiss parameter^{13,14}, at $t = 0$ (Figure 2b, left). We then advect these contours to $t = 50$ (Figure 2b, right). Clearly, the Okubo–Weiss zero curves deform significantly, and hence cannot be considered as approximations to coherent material vortex boundaries. This is in line with similar observations made by earlier studies (see, e.g., Pasquero et al.³³, Isern-Fontanet et al.³⁴, Henson and Thomas³⁵ and Beron-Vera et al.¹⁷). We present the definition and a detailed analysis of the Okubo–Weiss parameter in Section III D.

Returning to the analysis of the elliptic LCSs, figure 3 shows the relative stretching $\delta\ell(t) := (\ell(t) - \ell(a))/\ell(a)$ of the primary elliptic LCSs over the time interval $t \in [0, 50]$. Here, $\ell(t)$ denotes the length of a material line at time t . In principle, the initial and the final lengths of a primary elliptic LCS must be exactly equal, resulting in zero relative stretching at time $t = 50$. In practice, a deviation of at most 4% is observed from this ideal limit owing to numerical errors. The inset of figure 3 shows the relative stretching of a typical non-coherent iso-vorticity line. Unlike the coherent vortices, the relative stretching for a general material curve increases exponentially, with its final value at least an order of magnitude larger than that for a coherent vortex.

As mentioned in section §II, coherent material vortex boundaries are formed by a nested set of elliptic LCSs (i.e., closed λ -lines). Figure 4 shows two of the coherent vortices and their corresponding λ -lines. We find that for vortex 1, the secondary elliptic LCSs with $\lambda > 1$ lie in the interior of the primary elliptic LCS (i.e., the closed λ -line with $\lambda = 1$). For all other coherent vortices of figure 2, the secondary elliptic LCSs with $\lambda > 1$ lie in the exterior of the primary elliptic LCS. In all five cases, values of λ for which an elliptic LCS exists are close to 1, ranging in the interval $0.94 \leq \lambda \leq 1.05$.

The majority of vortices appearing in figure 2 are not coherent in the Lagrangian frame, and hence no elliptic LCSs were found around them. Some of the non-coherent vortices are trapped in a hyperbolic region, experiencing substantial straining over time. Others undergo a merger process where a larger vortex is created from two smaller co-rotating vortices. Each smaller vortex deforms substantially during the merger. The merged vortex may or may not

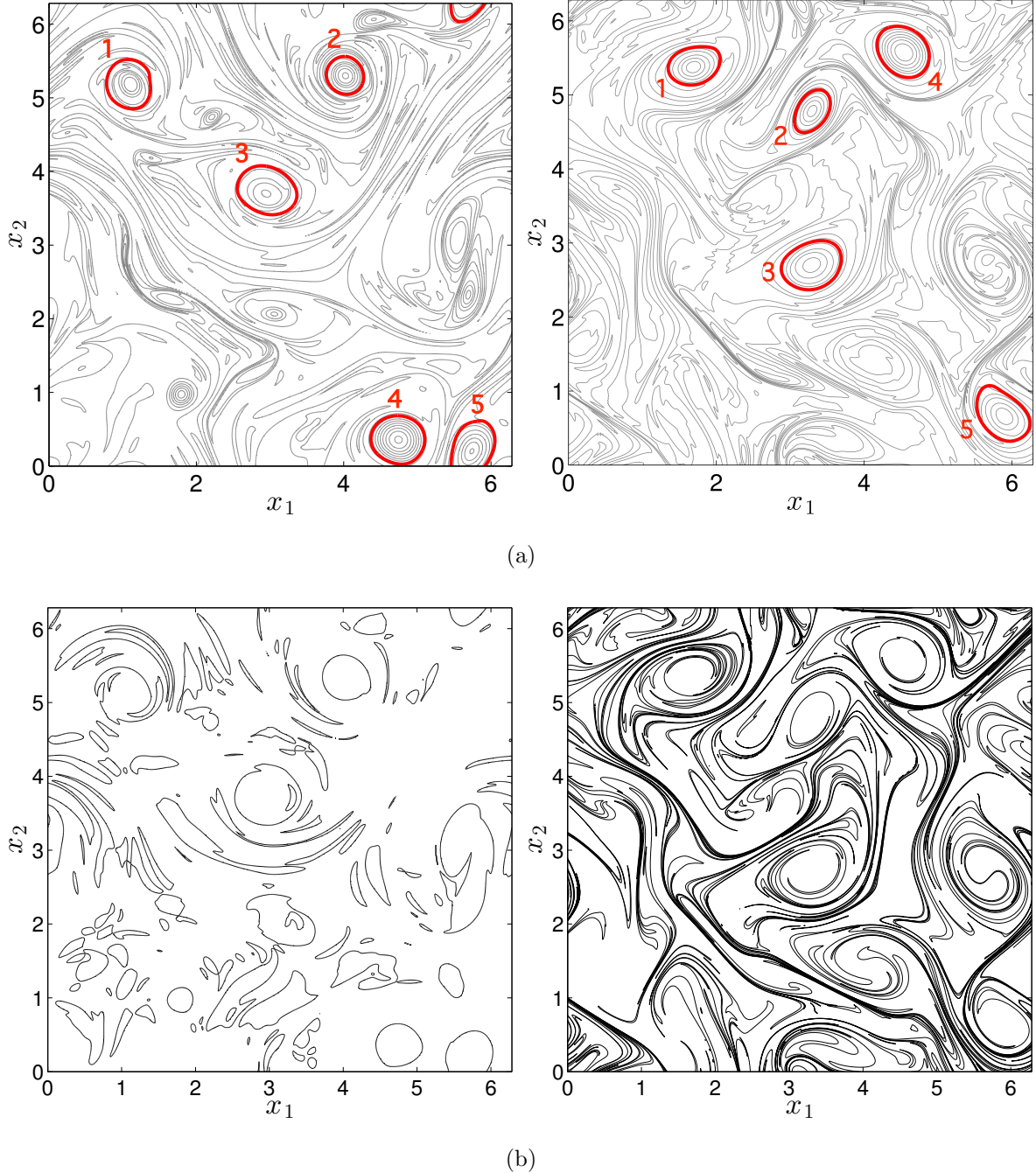


FIG. 2: (a) Lagrangian vortex boundaries (red) at time $t = 0$ (left) and $t = 50$ (right). The vorticity contours are shown in gray in the background. The vorticity contours are distributed as $-1 : 0.1 : 1$ at time $t = 0$ and as $-1.5 : 0.15 : 1.3$ at time $t = 50$. The coherent vortices are numbered in order to facilitate their identification at the two time-instances. (multimedia view) (b) Zero level curves of the Okubo-Weiss parameter at $t = 0$ (left) and their advected positions at time $t = 50$ (right).

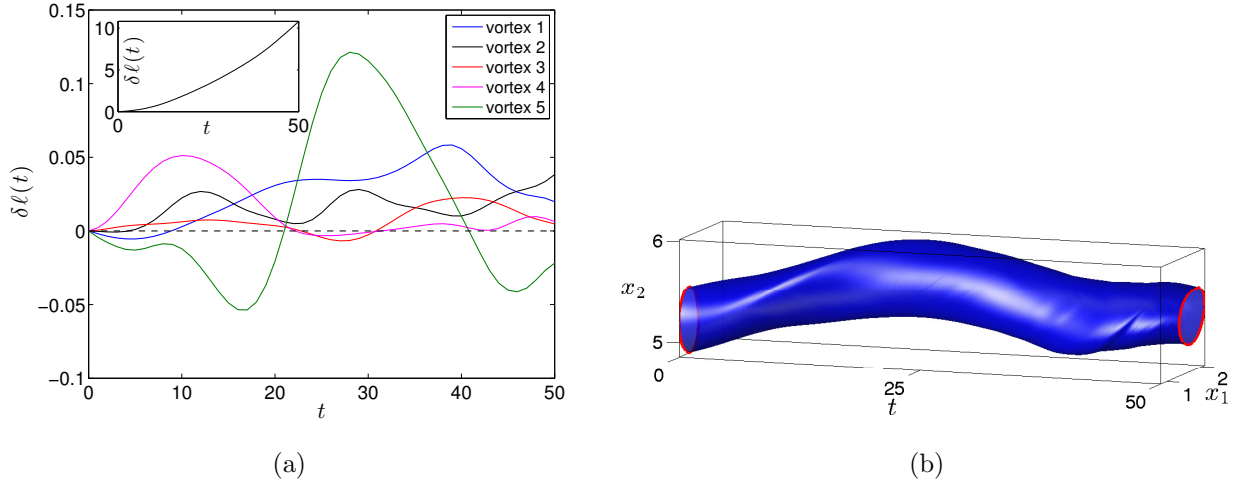


FIG. 3: (a) The relative deformation $\delta \ell$ as a function of time for the primary elliptic LCSs. The inset shows the relative stretching for a typical closed material line over the same time interval. (b) The Lagrangian vortex 1 in the extended phase space. The tube is created from the advection of the vortex boundary under the flow.

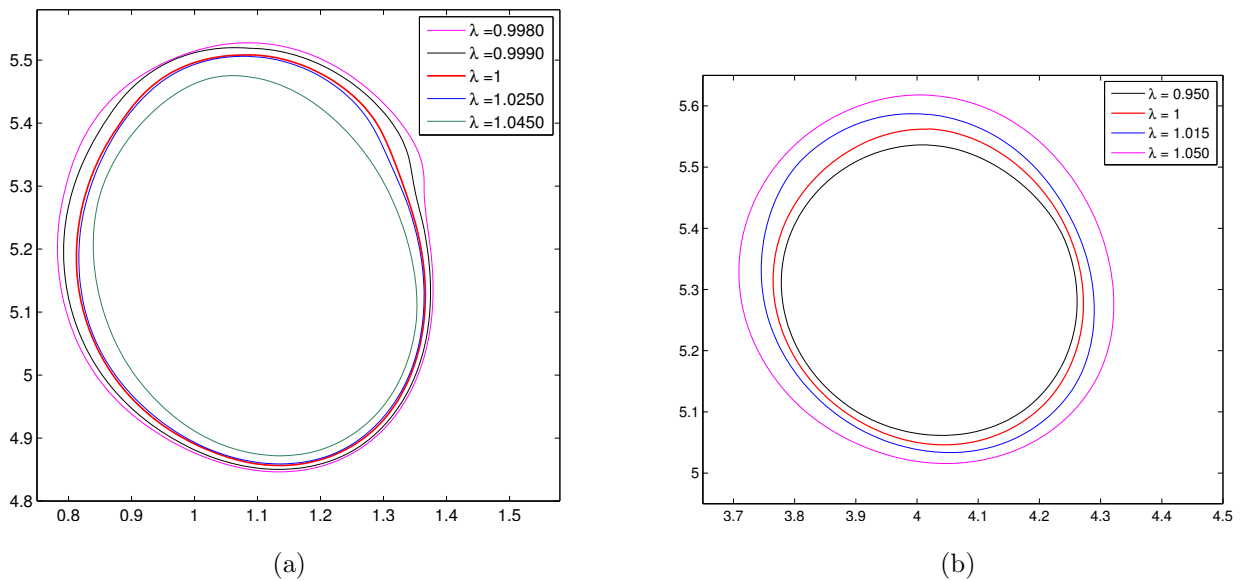


FIG. 4: Elliptic LCSs (i.e., closed λ -lines) around vortex 1 (a) and vortex 2 (b).

remain coherent for later times.

Figure 5 focuses on one Eulerian vortex undergoing a merger process. To illustrate the deformation of this vortex, we take three vorticity contours at time $t = 0$ near the center of the vortex. Selected vorticity contours are then advected to the final time $t = 50$, showing

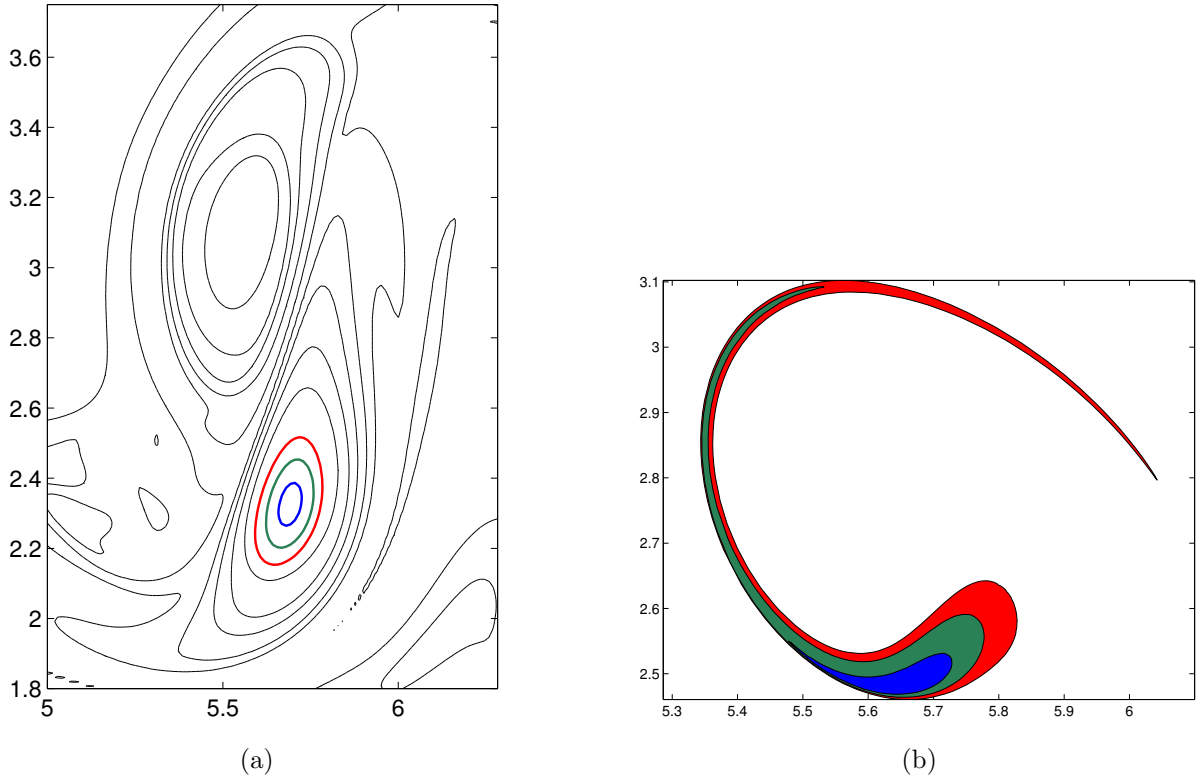


FIG. 5: (a) Vortex contours at $t = 0$ for two non-coherent vortices that merge as one later in time. To demonstrate the deformation of the vortices we monitor the advection of three vorticity contours. The contour values are 0.6 (red), 0.7 (green) and 0.8 (blue). (b) The selected contours advected to time $t = 50$ and filled with their corresponding color.

the resulting deformation of the vortex core. Figure 6 shows a similar analysis for a non-coherent vortex trapped in a uniformly hyperbolic region of the flow. Hyperbolicity produces stretching of vorticity gradients resulting in smearing of the vortex.

Figure 7 shows the generalized stable and unstable manifolds obtained by the geodesic theory of Lagrangian coherent structures^{22,36}, using the computational method described in Farazmand and Haller³⁷. These stable and unstable manifolds are, respectively, the most repelling and attracting material lines that form the skeleton of turbulent mixing patterns. The exponential attraction and repulsion generated by these manifolds leads to smearing of most fluid regions that appear as vortices in instantaneous streamline and vorticity plots. By contrast, the coherent Lagrangian vortices we identify remain immune to straining.

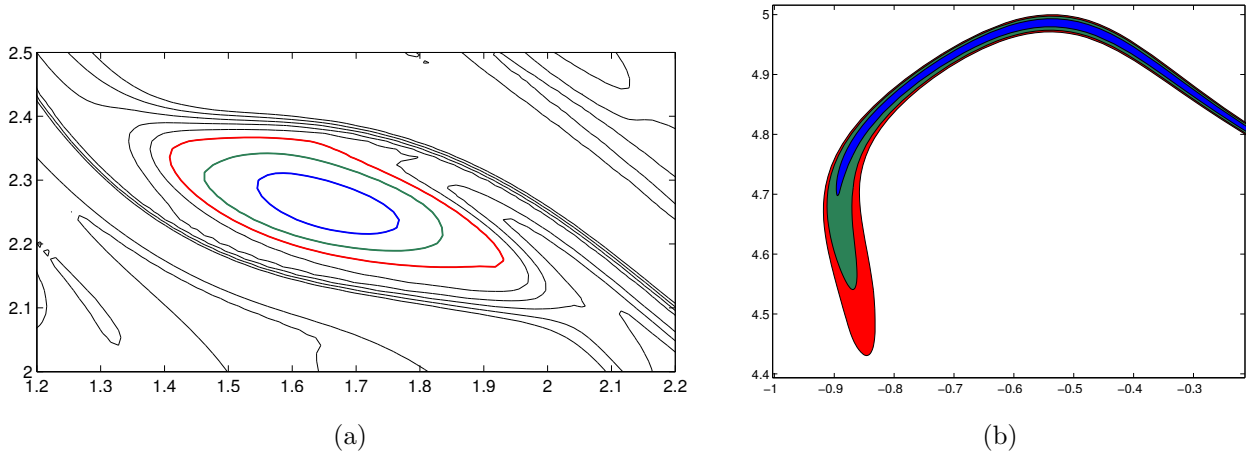


FIG. 6: (a) Vortex contours at $t = 0$ for a non-coherent vortex trapped in a straining field. The contours of vorticity with values 0.25 (red), 0.3 (green) and 0.35 (blue) are marked. (b) The selected contours advected to time $t = 50$ and filled with their corresponding color. Only part of the advected image is shown.

C. Optimality of coherent vortex boundaries

Here we examine the optimality of vortex boundaries obtained as outermost elliptic LCSs. The optimal boundary of a coherent vortex can be defined as a closed material line that encircles the largest possible area around the vortex and shows no filamentation over the observational time period. We seek to illustrate that outermost elliptic LCSs mark such optimal boundaries.

To this end, we consider a class of perturbations to the outermost elliptic LCS of vortex 1 corresponding to $\lambda = 0.998$. The perturbations are in the direction of the outer normal of the elliptic LCS. The amount of perturbation ranges between 0.01 and 0.06 (i.e., 1.5% to 10% of the diameter of the elliptic LCS). We then advect the vortex boundary and its perturbations to the final time $t = 50$ (see figure 8b). The perturbed curves visibly depart from the coherent core marked by the red elliptic LCS. Our findings are similar for all other coherent vortices (not shown here).

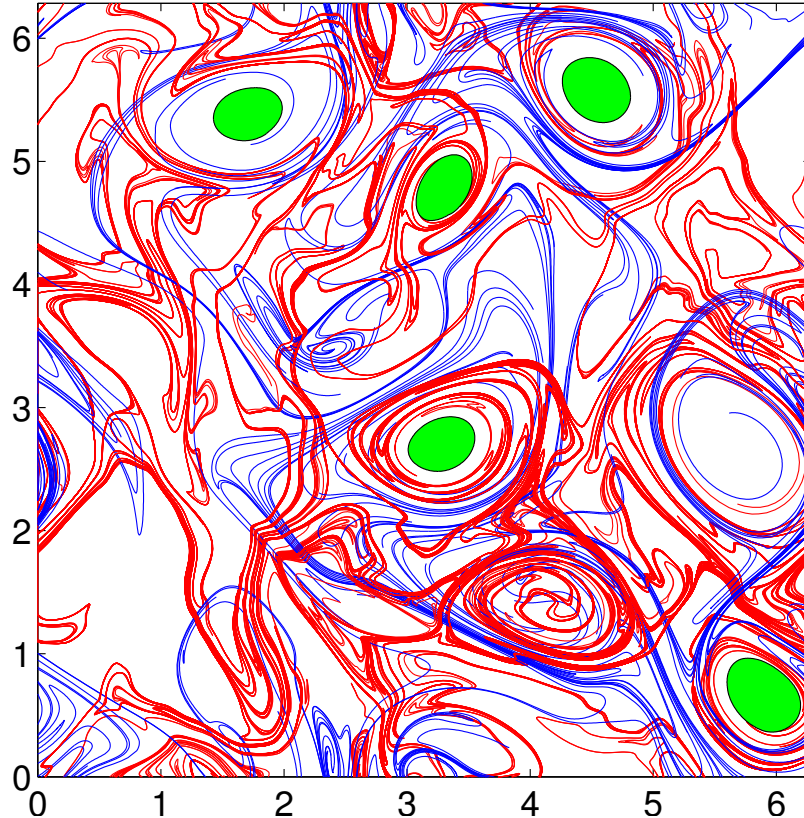


FIG. 7: Generalized stable (red) and unstable (blue) manifolds. The coherent Lagrangian vortices (green), i.e. generalized KAM regions, are not penetrated by these manifolds. The manifolds and the KAM regions are shown at $t = 50$.

D. Comparison with Eulerian and Lagrangian vortex indicators

Several diagnostics have been previously proposed to identify vortex boundaries. Among the Eulerian indicators are the vorticity criterion of McWilliams³⁸, the Okubo-Weiss (OW) criterion^{13,14} and the modified OW criterion of Hua and Klein¹⁶. These Eulerian methods are non-objective (frame-dependent), instantaneous in nature, and are generally used in practice with tunable thresholds. For all these reasons, they have little chance to capture long-term coherence in the Lagrangian frame. Nevertheless, they are broadly believed to be good first-order indicators of coherence in the flow.

We find that the coherent vortex boundaries obtained as outermost elliptic LCSs cannot be approximated by the instantaneous vorticity contours at the initial time $t = 0$. Figure 9 compares these vortex boundaries with the vorticity contours for two of the coherent vortices. None of the vorticity contours approximates the actual observed coherent vortex

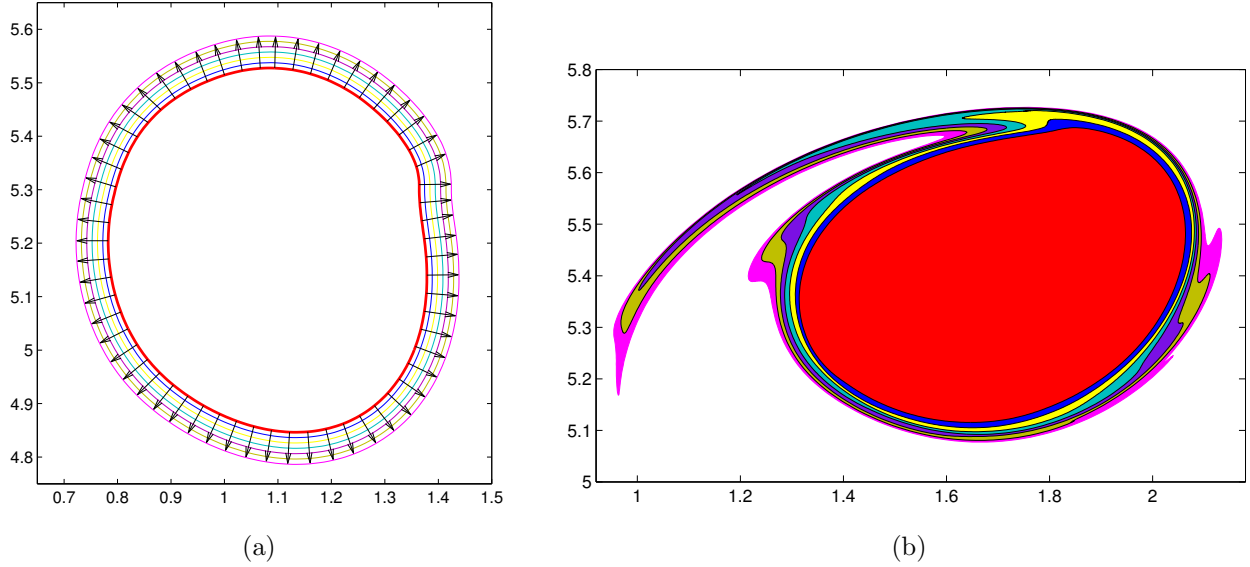


FIG. 8: (a) The outermost elliptic LCS (red) encircling vortex 1 of figure 2 and its outer normal perturbations. The perturbation parameter ranges between 0.01 and 0.06. (b) The advected image of the elliptic LCS and its normal perturbations at time $t = 50$. Each advected image is filled with its corresponding color from panel (a)

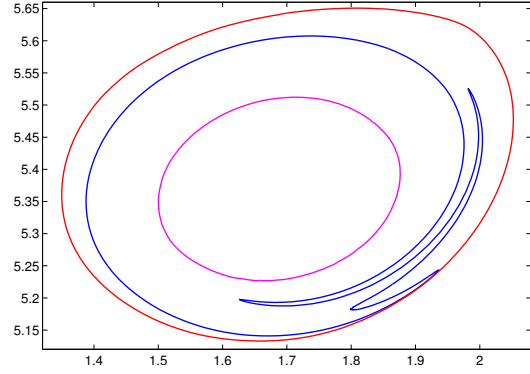
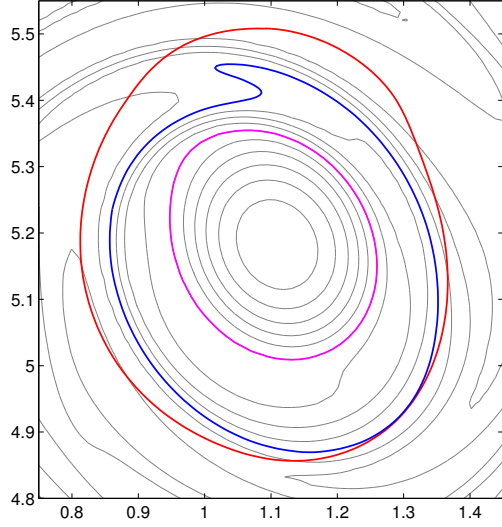
boundary of the Lagrangian frame. In fact, the nearby vorticity contours are not axisymmetric, even though that is intuitively expected for a coherent vortex boundary³⁸. For instance, the closest vorticity contour to the elliptic LCSs (blue curves in Fig. 9) notably lack axisymmetry. Their advected positions at time $t = 50$ develop filaments. In contrast, the magenta-colored axisymmetric contours closest to the elliptic LCS preserve their overall shape. These contours would, however, significantly underestimate the true extent of the coherent fluid region.

Similar observations can be made for the OW criterion. The OW parameter

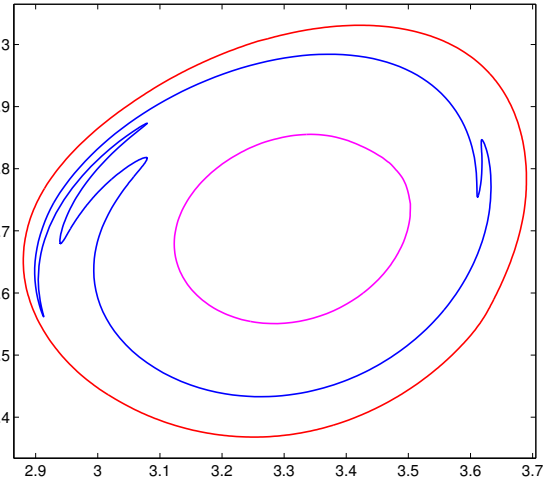
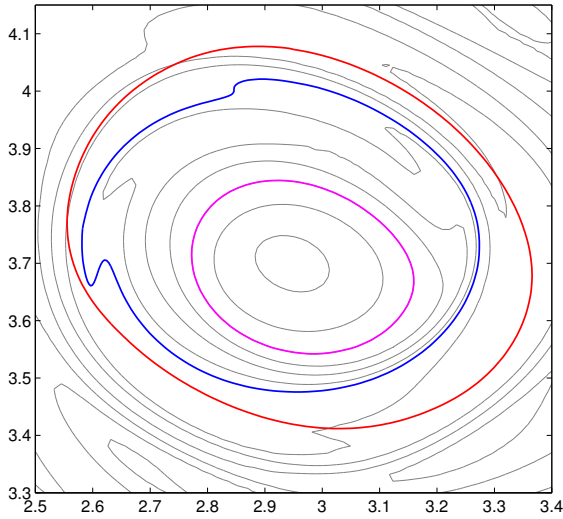
$$Q = |S|^2 - |\Omega|^2, \quad (8)$$

measures instantaneous straining against instantaneous rotation. Here, S and Ω are, respectively, the symmetric and anti-symmetric parts of the velocity gradient ∇u . The matrix norms involved are computed as $|S|^2 = (\partial_1 u_1 - \partial_2 u_2)^2 + (\partial_1 u_2 + \partial_2 u_1)^2$ and $|\Omega|^2 = \omega^2$, where (u_1, u_2) are the components of the velocity field and $\omega = \partial_1 u_2 - \partial_2 u_1$ is the vorticity field.

The subset of the domain where $Q > 0$ is dominated by strain, while $Q < 0$ marks the regions dominated by vorticity. Thus, the zero contour of this parameter encircling a



(a)



(b)

FIG. 9: (a) Left: Vorticity contours (gray) and the Lagrangian vortex boundary (red) for vortex 1 at time $t = 0$. The blue curve marks the closed vorticity contour that lays entirely inside the elliptic LCS. This contour corresponds to $\omega = -0.3$. The magenta curve marks the closest axisymmetric vorticity contour to the elliptic LCS. Right: The Lagrangian vortex boundary and selected vorticity contours advected to time $t = 50$. (b) Same as (a) for vortex 3. The contour marked by the blue curve corresponds to $\omega = -0.32$.

vortex may be expected to mark the outermost boundary of the vortical region. Several authors have noted, however, that the zero contours of Q will not necessarily mark vortex-like structures (see, e.g., Pasquero et al.³³ and Koszalka et al.³⁹).

In practice, a negative-valued contour of Q satisfying $Q = -\alpha\sigma_Q$ is often considered as the vortex boundary³³, where α is a positive constant and σ_Q is the standard deviation of the spatial distribution of Q . The constant α is somewhat arbitrary and must be tuned for a particular flow. Pasquero et al.³³, Isern-Fontanet et al.³⁴ and Henson and Thomas³⁵, for instance, use $\alpha = 0.2$ while Koszalka et al.³⁹ use $\alpha = 1$.

A closer inspection of figure 10 reveals that none of the OW contours approximate well the true coherent Lagrangian vortex boundary. The closest OW contour (blue curve) to the outermost elliptic LCS lacks axisymmetry and develops substantial filamentation under advection. The axisymmetric contour (magenta curve) contained in the coherent vortex preserves its shape but seriously underestimates the extent of the coherent region (as do axisymmetric vorticity contours). This axisymmetric contour of the OW parameter is also the outermost contour that remains in the $Q < 0$ region over the entire time interval $t \in [0, 50]$.

We obtain similar conclusions about other OW-type Eulerian indicators that have been developed to overcome the shortcomings of the OW criterion (see, e.g., Chong et al.¹⁵, Hua and Klein¹⁶, Tabor and Klapper⁴⁰, Kida and Miura⁴¹). Hua and Klein¹⁶, for instance, consider the effect of higher-order terms due to fluid acceleration. They arrive at the indicator parameters λ_{\pm} given by

$$\lambda_{\pm} = \frac{1}{4}Q \pm \frac{1}{2}\sqrt{|\dot{S}|^2 - |\dot{\Omega}|^2},$$

where \dot{S} and $\dot{\Omega}$ denote, respectively, the instantaneous rate of change of strain and vorticity along fluid trajectories. The scalar Q is the OW parameter, defined in (8). The positive extrema of λ_{+} correspond to regions of instantaneously strong stirring and dispersion. The negative extrema of λ_{-} , on the other hand, mark the vortex regions.

As in the case of vorticity and the OW-parameter, we find that the Lagrangian vortex boundaries cannot be inferred from the contours of the λ_{\pm} parameters (see figure 11). The axisymmetric contours of λ_{\pm} remain coherent under material advection over the time interval $t \in [0, 50]$. They, however, are significantly smaller (in enclosed surface area) than the true Lagrangian vortex boundary marked by the elliptic LCS.

The last Eulerian indicator we consider here is the streamline-based eddy detection method proposed by Servidio et al.⁴². This method uses the topography of the instantaneous stream function $\psi = -\Delta^{-1}\omega$ to locate a vortex. Specifically, a streamline-based vortex boundary is locally the largest closed, numerically computed streamline that does not

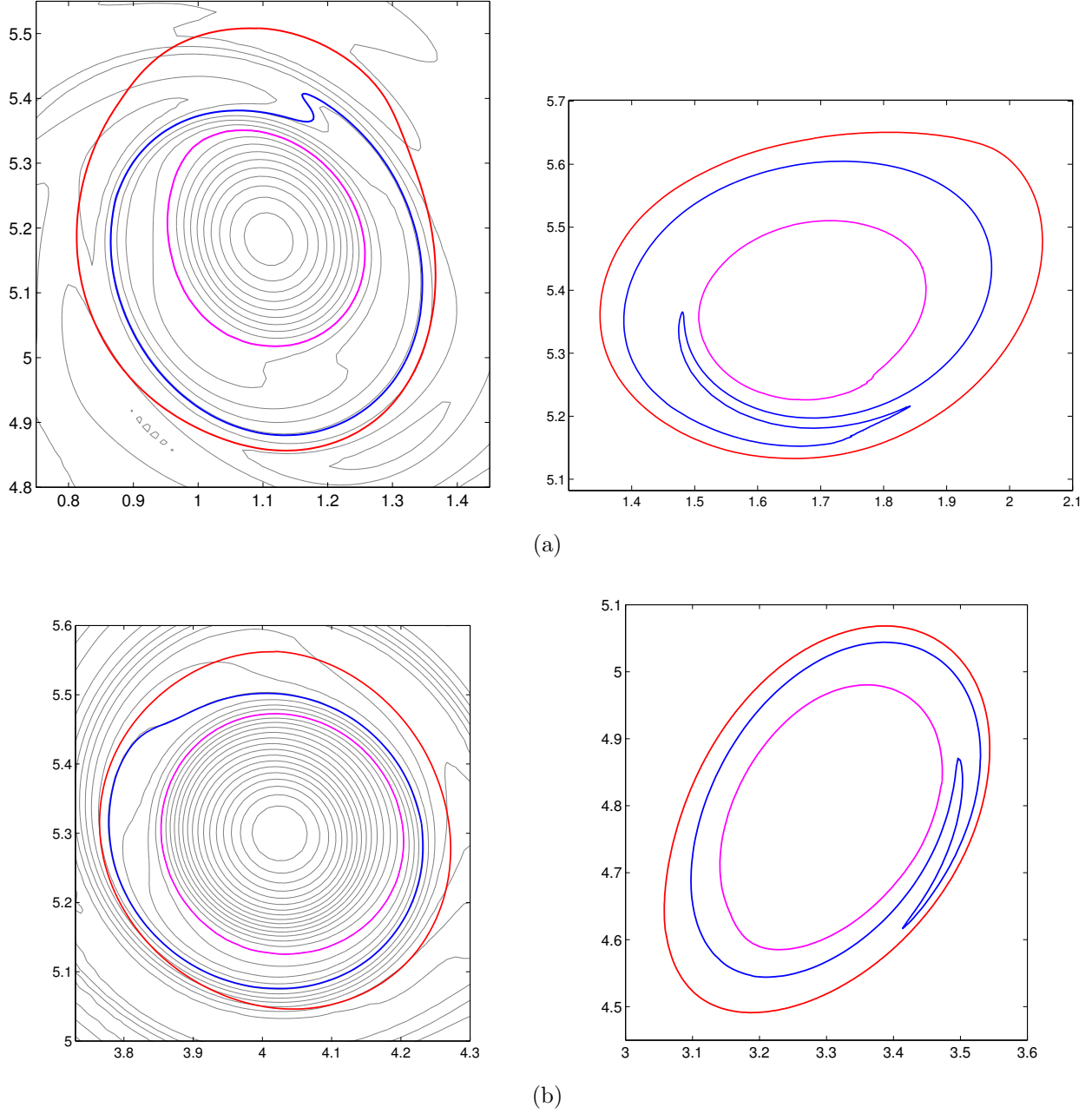


FIG. 10: (a) Left: OW contours (gray) and the Lagrangian vortex boundary (red) for vortex 1 at time $t = 0$. Two contours corresponding to $Q = -0.072 \simeq -0.97\sigma_Q$ (blue) and $Q = -0.240 \simeq -3.22\sigma_Q$ (magenta) are selected for advection. Right: The Lagrangian vortex boundary and selected OW contours advected to time $t = 50$. (b) Same as (a) for vortex 2. Here, the OW contours corresponding to $Q = -0.096 \simeq -1.29\sigma_Q$ (blue) and $Q = -0.40 \simeq -5.36\sigma_Q$ (magenta) are selected for advection.

enclose a saddle point. Figure 12 shows the eddies detected in this fashion. The approach

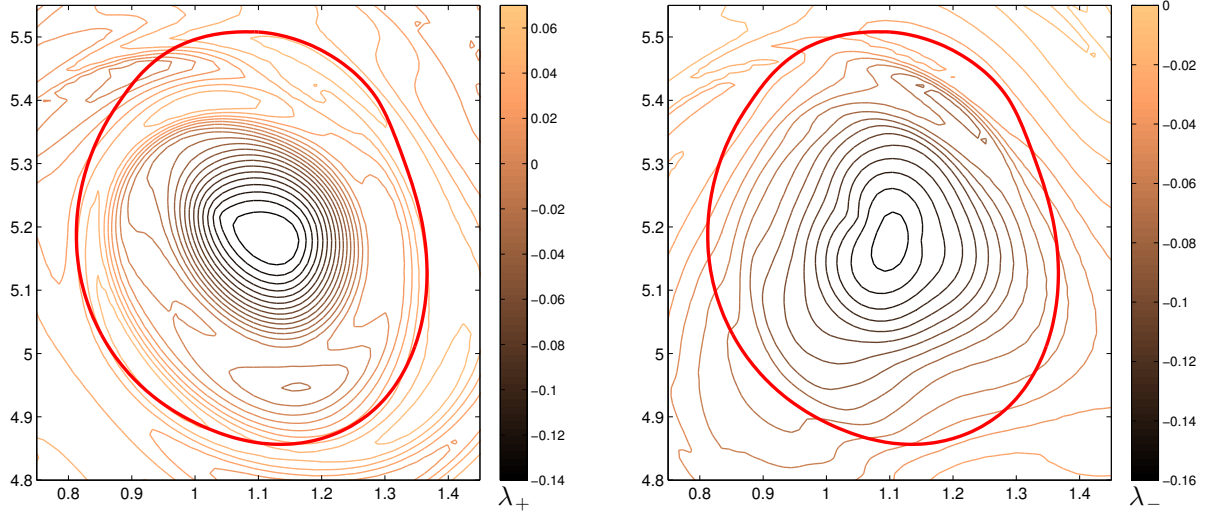


FIG. 11: The contours of λ_+ (left) and λ_- (right) around vortex 1 at time $t = 0$. The Lagrangian vortex boundary is shown with thick red line.

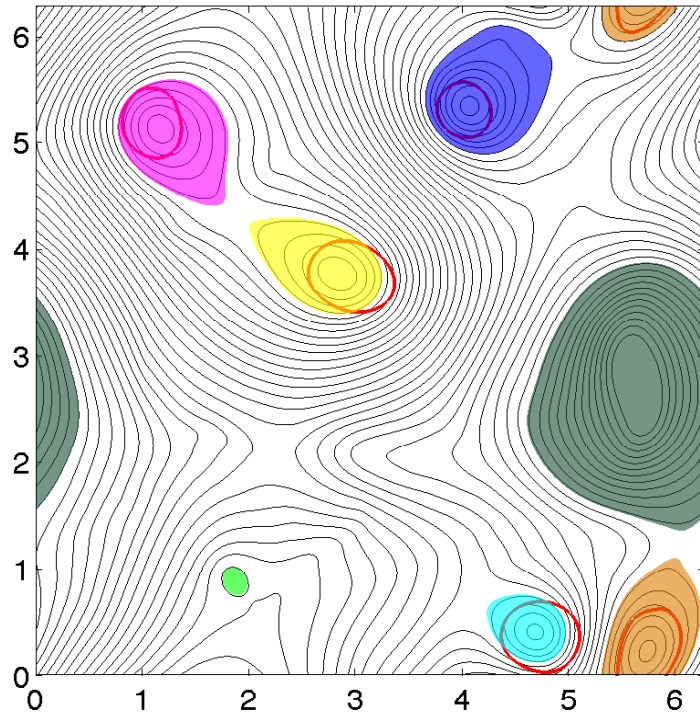


FIG. 12: Streamline-based eddies (colored patches), Lagrangian vortex boundaries (red curves) and the streamlines (black curves) at the initial time $t = 0$.

can be automated using a cellular automata algorithm (see Servidio et al. ⁴², Appendix A).

As noted by Servidio et al.⁴², the streamline-based eddy detection method seeks regions where strong vortical structures may exist. Thus, each eddy island may, in principle, contain more than one vortex, as is indeed the case for the dark green island of figure 12. Obtained from the instantaneous stream function, however, the detected eddies are not guaranteed to preserve their shape under advection. For instance, the (dark and light) green patches quickly filament under advection.

Interestingly, the streamline-based eddy detection also misses parts of the vortical structures: some of the Lagrangian coherent vortices are not completely contained in streamline-based eddy regions. This is the case for the vortices intersecting the yellow- and cyan-colored patches in figure 12. Other Lagrangian coherent vortices happen to be fully contained in the blue-, magenta- and brown-colored patches.

Compared to the number of Eulerian criteria, there are far fewer Lagrangian diagnostics developed for quantifying coherent vortices. These include the finite-time Lyapunov exponent^{43,44}, mesoellipticity⁴⁵, relative coherent pairs^{46,47}, shape coherence⁷ and the ergodic partition of time-averaged observables⁴⁸. Here we evaluate the performance of two of these in coherent Lagrangian vortex detection: finite-time Lyapunov exponents and mesoellipticity.

The finite-time Lyapunov exponent (FTLE) measures the maximal local stretching of material lines. For any point $x_a \in U$, the FTLE corresponding to a time interval $[a, b]$ is defined as

$$\Lambda(x_a) = \frac{1}{2(b-a)} \log(\lambda_2(x_a)), \quad (9)$$

where λ_2 is the larger eigenvalue of the Cauchy–Green strain tensor C . The FTLE measures the maximum separation of nearby initial conditions over $[a, b]$. Therefore, its higher values suggest regions of high stretching, and lower values generally indicate moderate stretching. One envisions that low-FTLE regions to coincide with the coherent Lagrangian vortex regions identified from our analysis.

Figure 13 shows color-coded FTLE values for vortices 1 and 2. Clearly, the Lagrangian vortex boundary (red curves) cannot be inferred from the FTLE plot. In fact, locally maximal values of FTLE spiral into the Lagrangian vortex boundary, giving the wrong impression that it will stretch significantly under advection.

In addition, FTLE contours around the vortex core lack axisymmetry. The outermost, almost-axisymmetric FTLE contours encircling the vortex cores (black curves) are still far

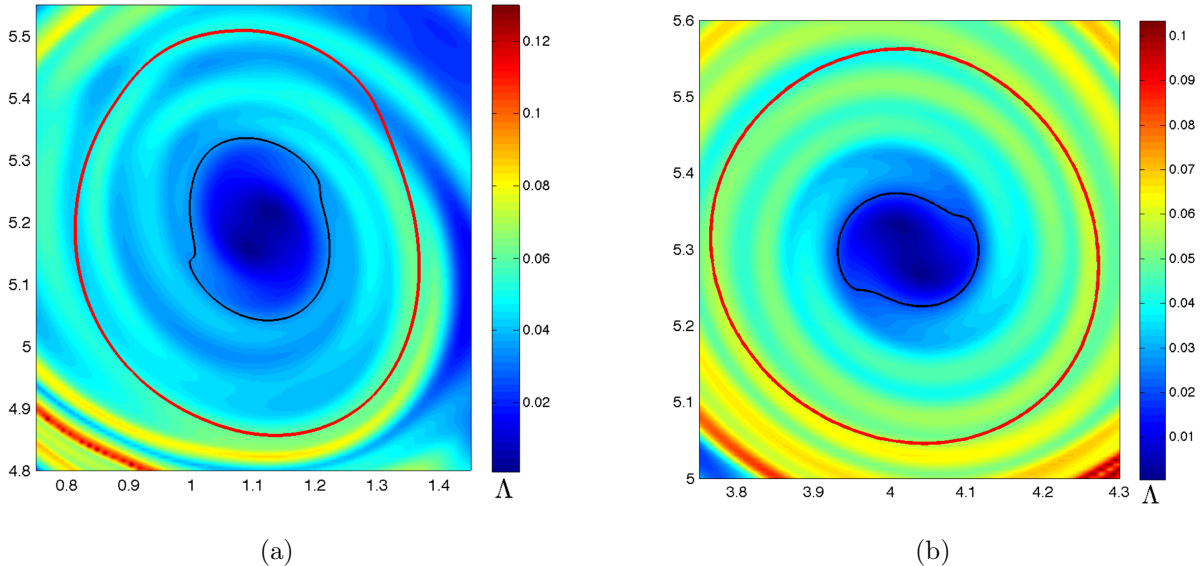


FIG. 13: (a) Time $t = 0$ position of the Lagrangian vortex boundary (red) for vortex 1. The background color shows the FTLE field. The black curve marks the FTLE contour with $\Lambda = 3.45 \times 10^{-2}$. The FTLE value is chosen such that the corresponding contour is the outermost, almost-axisymmetric contour encircling the vortex core. (b) Same as (a) for vortex 2. Here, the value of the FTLE contour is $\Lambda = 2.0 \times 10^{-2}$

from the true vortex boundary marked by the elliptic LCS.

Now we consider a comparison between elliptic LCSs and elliptic regions obtained from the Lagrangian mixing diagnostic of Mezić et al.⁴⁵. This diagnostic classifies a trajectory starting from a point x_a as *mesoelliptic* in an incompressible flow, if the eigenvalues of the deformation gradient $DF(x_a)$ lie on the complex unit circle. Mesoelliptic trajectories are expected to lie in a vortical region. In contrast, if the eigenvalues of $DF(x_a)$ are off the complex unit circle, the trajectory is classified as *mesohyperbolic* and is expected to lie in a strain-dominated region.

Figure 14 shows the hypergraph map⁴⁵ for our turbulent flow, marking mesoelliptic (green and white) and mesohyperbolic (yellow and blue) regions. As a rule, the actual Lagrangian coherent vortex boundaries (i.e., the outermost elliptic LCSs marked in red) always turn out to fall near the boundary of a mesoelliptic (blue) annulus. Similar mesoelliptic annuli regions exist, however, both inside and outside the Lagrangian vortex, thus an a priori identification of the coherent vortex boundary cannot be achieved based on mesoelliptic regions. Furthermore, substantial portions of the actual Lagrangian vortices are diagnosed

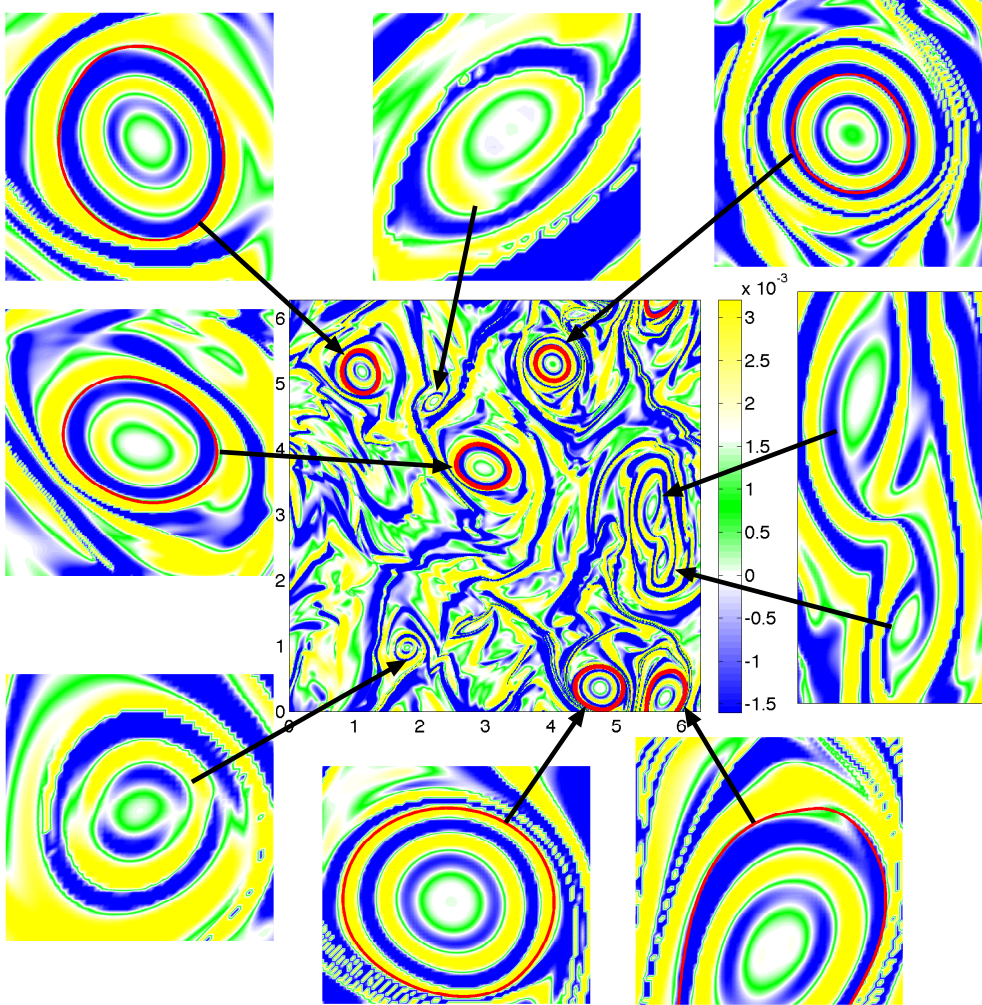


FIG. 14: Hypergraph map for the turbulent flow marking mesohyperbolic (yellow and blue color) and mesoelliptic (green and white) regions. The outermost elliptic LCSs are shown as red curves. The three magnified regions, where elliptic LCSs are absent, show examples of mesoelliptic regions undergoing large stretching.

as mesohyperbolic (annular yellow and blue regions). Likewise, a number of mesoelliptic regions appear in non-coherent, hyperbolic mixing domains (compare with figure 7). These mesoelliptic areas undergo substantial stretching and filamentation, and hence are false positives in coherent vortex detection. We conclude that a systematic, a priori identification of coherent Lagrangian vortex boundaries from mesoellipticity is not possible in our turbulent flow.

IV. CONCLUSIONS

We have used the variational theory of Haller and Beron-Vera⁶ to detect coherent material vortices in a direct numerical simulation of two-dimensional Navier–Stokes turbulence. We demonstrated that the vortex boundaries so obtained are optimal in the sense that they are the outermost material lines enclosing a vortex and retaining their shapes over long time intervals. They are also frame-independent, threshold-free and Lagrangian by construction.

A comparison with other Eulerian methods (vorticity contours, the Okubo–Weiss criterion, and the Hua–Klein criterion) shows that the size of coherent material vortices in turbulence is substantially larger than previously inferred from Eulerian indicators. At the same time, the number of coherent vortices is lower than what is signaled by the same indicators. This is consistent with the findings in Beron-Vera et al.¹⁷, who observed a similar trend for ocean eddies in satellite-altimetry-based velocity fields of the South Atlantic. We find that the superfluous vortices suggested by Eulerian indicators are destroyed relatively quickly by the straining induced by repelling and attracting Lagrangian coherent structures present in the flow.

We also compared our results with two Lagrangian indicators: the finite-time Lyapunov exponent (FTLE) and the mesoellipticity diagnostic of Mezić et al.⁴⁵. Low FTLE values generally indicate the approximate position of vortex cores but do not provide an indication of coherent Lagrangian vortex boundaries. Furthermore, FTLE lows also occur in incoherent vortical regions as well, thus its use leads to false positives in coherent material vortex detection.

As a rule, mesoelliptic annuli tend to form near the coherent Lagrangian vortex boundaries. However, such annuli also form both inside and outside coherent vortices, as well as in hyperbolic mixing regions. Therefore, an accurate and a priori identification of coherent Lagrangian vortices from mesoellipticity was not possible.

Compared to instantaneous Eulerian indicators, such as Okubo-Weiss criterion, Lagrangian vortex detection is clearly computationally more expensive. It requires accurate advection of a large ensemble of fluid particles, as well as closed orbit detection in the vector fields (6). Therefore, developing cost effective computational algorithms while staying faithful to the underlying theory is of great interest (see Leung⁴⁹, Shadden⁵⁰, Peikert et al.⁵¹, for recent developments).

Future theoretical work will focus on the correlation between Lagrangian coherent vortices and the dynamical properties of the flow, e.g., the scale-by-scale transfer of energy and enstrophy⁵².

The streamline-based eddy detection discussed in Section III.D was originally developed to study the formation of coherent structures in decaying two-dimensional turbulence. Servidio et al. Servidio et al.⁴² show that the local relaxation to coherent structures is tied to the system’s tendency to maximize a local notion of entropy. It is of interest to re-examine this observation by adopting the more accurate description of coherent vortices used in the present paper.

ACKNOWLEDGMENTS

We would like to thank Jan Feys for his help with the implementation of the Fourier transform in MATLAB. We also thank Daniel Blazeovski for sharing his code for generating the hypergraph map of figure 14.

REFERENCES

- ¹A. Provenzale. Transport by coherent barotropic vortices. *Ann. Rev. Fluid Mech.*, 31: 55–93, 1999.
- ²H. Kellay and W. I. Goldburg. Two-dimensional turbulence: a review of some recent experiments. *Reports on Progress in Physics*, 65(5):845, 2002.
- ³A. Provenzale, A. Babiano, A. Bracco, C. Pasquero, and J. B. Weiss. Coherent vortices and tracer transport. In *Transport and Mixing in Geophysical Flows, Lecture Notes in Physics*, pages 101–118. Springer, 2008.
- ⁴G. Boffetta and R. E. Ecke. Two-dimensional turbulence. *Ann. Rev. Fluid Mech.*, 44: 427–451, 2012.
- ⁵H. E. Fiedler. Coherent structures in turbulent flows. *Prog. in Aerospace Sci.*, 25:231–269, 1988.
- ⁶G. Haller and F. J. Beron-Vera. Coherent Lagrangian vortices: The black holes of turbulence. *J. Fluid Mech.*, 731, R4, 2013.

- ⁷T. Ma and E. M. Bollt. Differential geometry perspective of shape coherence and curvature evolution by finite-time non-hyperbolic splitting. *arXiv preprint arXiv:1311.5457*, 2013.
- ⁸U. Frisch. *Turbulence: the legacy of A.N. Kolmogorov*. Cambridge University Press, 1995.
- ⁹J. C. McWilliams. *Fundamentals of geophysical fluid dynamics*. Cambridge University Press, 2006.
- ¹⁰M. E. Gurtin. *An introduction to continuum mechanics*. Volume 158 of Mathematics in Science and Engineering. Academic Press, 1981.
- ¹¹J. Jeong and F. Hussain. On the identification of a vortex. *J. of Fluid Mech.*, 285:69–94, 1995.
- ¹²G. Haller. An objective definition of a vortex. *J. Fluid Mech.*, 525:1–26, 2005.
- ¹³A. Okubo. Horizontal dispersion of floatable particles in the vicinity of velocity singularities such as convergences. *Deep Sea Research*, 17:445–454, 1970.
- ¹⁴J. Weiss. The dynamics of enstrophy transfer in two-dimensional hydrodynamics. *Physica D*, 48:273–294, 1991.
- ¹⁵M. S. Chong, A. E. Perry, and B. J. Cantwell. A general classification of three-dimensional flow fields. *Phys. fluids A*, 2(5):765–777, 1990.
- ¹⁶B. L. Hua and P. Klein. An exact criterion for the stirring properties of nearly two-dimensional turbulence. *Physica D*, 113(1):98–110, 1998.
- ¹⁷F. J. Beron-Vera, Y. Wang, M. J. Olascoaga, G. J. Goni, and G. Haller. Objective detection of oceanic eddies and the Agulhas leakage. *J. of Phys. Oceanogr.*, 43(7), 2013.
- ¹⁸V. I. Arnold. *Mathematical Methods of Classical Mechanics*. Springer, 1978.
- ¹⁹H. Aref. Stirring by chaotic advection. *J. Fluid Mech.*, 143:1–21, 1984.
- ²⁰C. Truesdell and W. Noll. *The non-linear field theories of mechanics*. Springer, New York, third edition, 2004.
- ²¹J. Guckenheimer and P. Holmes. *Nonlinear oscillations, dynamical systems, and bifurcations of vector fields*, volume 42. New York, Springer Verlag, 1983.
- ²²G. Haller and F. J. Beron-Vera. Geodesic theory of transport barriers in two-dimensional flows. *Physica D*, 241(20):1680 – 1702, 2012.
- ²³A. Hadjighasem, M. Farazmand, and G. Haller. Detecting invariant manifolds, attractors, and generalized KAM tori in aperiodically forced mechanical systems. *Nonlinear Dynamics*, 73(1-2):689–704, 2013.
- ²⁴J. Beem, P. Ehrlich, and K. Easley. Global Lorentzian geometry, volume 202 of monographs

- and textbooks in pure and applied mathematics, 1996.
- ²⁵D. Karrasch, F. Huhn, and G. Haller. Automated detection of coherent Lagrangian vortices in two-dimensional unsteady flows. *arXiv preprint arXiv:1404.3109*, 2014.
- ²⁶C.-M. Claudel, K. S. Virbhadra, and G. F. R. Ellis. The geometry of photon surfaces. *J. Math. Phys.*, 42:818–838, 2001.
- ²⁷J. R. Dormnad and P. J. Prince. A family of embedded Runge-Kutta formulae. *J. Comp. Appl. Math.*, 6:19–26, 1980.
- ²⁸R. H. Kraichnan. Inertial ranges in two-dimensional turbulence. *Phys. Fluids*, 10:1417–1423, 1967.
- ²⁹P. E. Merilees and H. Warn. On energy and enstrophy exchanges in two-dimensional non-divergent flow. *J. Fluid Mech.*, 69:625–630, 1975.
- ³⁰G. Boffetta, A. Celani, S. Musacchio, and M. Vergassola. Intermittency in two-dimensional Ekman–Navier-Stokes turbulence. *Phys. Rev. E*, 66:026304, 2002.
- ³¹Y.-K. Tsang, E. Ott, T. M. Antonsen, and P. N. Guzdar. Intermittency in two-dimensional turbulence with drag. *Phys. Rev. E*, 71:066313, 2005.
- ³²M. Farazmand and G. Haller. Computing Lagrangian Coherent Structures from their variational theory. *Chaos*, 22:013128, 2012.
- ³³C. Pasquero, A. Provenzale, and A. Babiano. Parameterization of dispersion in two-dimensional turbulence. *J. Fluid Mech.*, 439:279–303, 2001.
- ³⁴J. Isern-Fontanet, E. García-Ladona, and J. Font. Vortices of the Mediterranean sea: An altimetric perspective. *J. Phys. Oceanogr.*, 36(1), 2006.
- ³⁵S. A. Henson and A. C. Thomas. A census of oceanic anticyclonic eddies in the Gulf of Alaska. *Deep Sea Research*, 55(2):163 – 176, 2008.
- ³⁶M. Farazmand, D. Blazeovski, and G. Haller. Shearless transport barriers in unsteady two-dimensional flows and maps. *Physica D*, 278-279:44–57, 2014.
- ³⁷M. Farazmand and G. Haller. Attracting and repelling Lagrangian coherent structures from a single computation. *Chaos*, 23:023101, 2013.
- ³⁸J. C. McWilliams. The vortices of two-dimensional turbulence. *J. Fluid Mech.*, 219:361–385, 1990.
- ³⁹I. Koszalka, A. Bracco, J. C. McWilliams, and A. Provenzale. Dynamics of wind-forced coherent anticyclones in the open ocean. *J. Geophys. Res.*, 114, 2009.
- ⁴⁰M. Tabor and I. Klapper. Stretching and alignment in chaotic and turbulent flows. *Chaos*,

- Solitons & Fractals*, 4(6):1031 – 1055, 1994.
- ⁴¹S. Kida and H. Miura. Identification and analysis of vortical structures. *European Journal of Mechanics - B/Fluids*, 17(4):471 – 488, 1998.
- ⁴²S. Servidio, M. Wan, W. H. Matthaeus, and V. Carbone. Local relaxation and maximum entropy in two-dimensional turbulence. *Phys. Fluids*, 22:125107, 2010.
- ⁴³J. M. Ottino. *The kinematics of mixing: stretching, chaos and transport*. Cambridge University Press, 1989.
- ⁴⁴R. T. Pierrehumbert and H. Yang. Global chaotic mixing on isentropic surfaces. *J. Atmos. Sci.*, 50:2462–2480, 1993.
- ⁴⁵I. Mezić, S. Loire, V. A. Fonoberov, and P. Hogan. A new mixing diagnostic and Gulf oil spill movement. *Science*, 330(6003):486–489, 2010.
- ⁴⁶G. Froyland. An analytic framework for identifying finite-time coherent sets in time-dependent dynamical systems. *Physica D*, 250:1–19, 2013.
- ⁴⁷T. Ma and E. M. Bollt. Relatively coherent sets as a hierarchical partition method. *International Journal of Bifurcation and Chaos*, 23(07), 2013.
- ⁴⁸M. Budišić, R. Mohr, and I. Mezić. Applied Koopmanism. *Chaos*, 22(4):047510, 2012.
- ⁴⁹S. Leung. An Eulerian approach for computing the finite time Lyapunov exponent. *J. of Comp. Phys.*, 230(9):3500–3524, 2011.
- ⁵⁰S. C. Shadden. Lagrangian coherent structures. In *Transport and Mixing in Laminar Flows: From Microfluidics to Oceanic Currents*, edited by Roman Grigoriev, pages 59–89. Wiley, New York, 2011.
- ⁵¹R. Peikert, A. Pobitzer, F. Sadlo, and B. Schindler. A comparison of finite-time and finite-size Lyapunov exponents. *Topological Methods in Data Analysis and Visualization III*. Springer, 2014.
- ⁵²D. H. Kelley, M. R. Allshouse, and N. T. Ouellette. Lagrangian coherent structures separate dynamically distinct regions in fluid flows. *Phys. Rev. E*, 88:013017, 2013.